



**HAL**  
open science

## Fast time-domain laser Doppler vibrometry characterization of surface acoustic waves devices

Nikolay Smagin, Lyes Djoumi, Etienne Herth, Meddy Vanotti, Dame Fall,  
Virginie Patissier, Marc Duquennoy, Mohammadi Ouafrouh

### ► To cite this version:

Nikolay Smagin, Lyes Djoumi, Etienne Herth, Meddy Vanotti, Dame Fall, et al.. Fast time-domain laser Doppler vibrometry characterization of surface acoustic waves devices. *Sensors and Actuators A: Physical*, 2017, 264, pp.96–106. 10.1016/j.sna.2017.07.035 . hal-02392694

**HAL Id: hal-02392694**

**<https://hal.science/hal-02392694v1>**

Submitted on 18 Dec 2024

**HAL** is a multi-disciplinary open access archive for the deposit and dissemination of scientific research documents, whether they are published or not. The documents may come from teaching and research institutions in France or abroad, or from public or private research centers.

L'archive ouverte pluridisciplinaire **HAL**, est destinée au dépôt et à la diffusion de documents scientifiques de niveau recherche, publiés ou non, émanant des établissements d'enseignement et de recherche français ou étrangers, des laboratoires publics ou privés.

# Fast time-domain laser Doppler vibrometry characterization of surface acoustic waves devices

Nikolay Smagin <sup>a,\*</sup>, Lyes Djoumi <sup>b</sup>, Etienne Herth <sup>c</sup>, Meddy Vanotti <sup>b</sup>, Dame Fall <sup>a</sup>, Virginie Blondeau-Patissier <sup>b</sup>, Marc Duquennoy <sup>a</sup>, Mohammadi Ouafthouh <sup>a</sup>

<sup>a</sup> Univ. Valenciennes, CNRS, Univ. Lille, ISEN, Centrale Lille, UMR 8520 – IEMN, DOAE, F-59313 Valenciennes, France

<sup>b</sup> Institut FEMTO-ST, Université de Franche Comté, UBFC, CNRS UMR 6174-25044 Besançon cedex, France

<sup>c</sup> Centre de Nanosciences et de Nanotechnologies, CNRS UMR 9001, Univ. Paris-Sud, Université Paris-Saclay, C2N-Orsay, 91405 Orsay cedex, France

## Article info

### Keywords:

SAW sensors  
Radio-frequency (RF) Laser  
Doppler vibrometry  
Interdigital transducers  
Crosstalk

## Abstract

This paper explores experiments and an in-depth analysis of surface acoustic waves (SAW) imaging using scanning laser Doppler vibrometry. Optical measurements allow visualization of wave propagation and resonance patterns in SAW devices as well as the detection of loss sources and undesired responses, such as escaping acoustic beams, unwanted reflections and acoustic crosstalk. We also report the characterization of a gas sensor based on electro-acoustic delay lines operating at 78.8 MHz and featuring a maximum SAW amplitude of 0.6 nm due to 33 dBm burst excitation. In addition to conventional full C-Scan (3200 points) of the structure, we report a series of B-Scans (430 points) referenced to the device geometry. The latter provides the same valuable information on SAW device operation with more versatility for graphical analysis and more than 10 times faster measurement times. Such capabilities have implications for the engineering of acoustic and sensor applications. In order to extend the analysis of the performance of SAW sensors, we discuss different experimental approaches using numerical simulation, radiofrequency and interferometric measurements. The present study highlights several approved SAW device characterization techniques and methods, the means of their optimization as well as applications for improving SAW device performances.

## 1. Introduction

Surface acoustic wave (SAW) devices [1] such as SAW filters, delay lines and resonators are widely used in mobile, spatial and wireless communications due to their high performance, small size, and good reproducibility [2,3]. At the same time, SAW technology provides a platform for sensing physical parameters (e.g., temperature, pressure, and stress) as well as chemicals in the gaseous and/or fluidic states [4,5]. Important advantages of SAW sensors include high sensitivity, short response time, low cost, compatibility with modern fabrication technology, and planar structure [6].

Furthermore, the operational frequency of SAW devices can be set in a wide range (MHz–GHz) which aids the sensitivity tuning and opens the possibility of wireless operation [7,8]. These sensors are expected to fulfil the increasingly demanded high performance in industry, military, pollution and emissions control, combustion exhausts, and other disciplines where a harsh environment often imposes the exploitation of wireless measurements. As a result of

such stringent requirements on SAW sensor energy performance and autonomy, the optimization of SAW device structure and the minimization of acoustic losses are at research and development priority [9,10].

Although theoretical models of electro-acoustic devices are well established [11], much of the characterization procedures rely on measuring of the electrical response (e.g. S-parameter measurements) [9,12,13]. These standard electrical measurements provide important information about insertion losses, frequency band parameters (central frequency, Q-factor, secondary lobes), but nevertheless represent only secondary information on wave propagation and underlying physical processes. They do not therefore provide full insight into the device operation [14]. At the same time, optical probing methods enables direct measurement of the vibration fields without influencing device operation [14,15], while yieldings primary information of the wave physics and device performance. For example, imaging the wave field amplitude distributions in SAW devices can reveal possible sources of losses and unwanted responses, such as excitation of transverse modes, escaping acoustic beams in resonators or acoustic crosstalk in filters.

In state-of-the-art characterization, it is common to combine electrical testing with optical probing [16–18]. One of the most

\* Corresponding author.

E-mail address: [Nikolay.Smagin@univ-valenciennes.fr](mailto:Nikolay.Smagin@univ-valenciennes.fr) (N. Smagin).

widespread and accessible techniques of optical probing is Laser Doppler vibrometry (LDV) [19], which allows the measurement of the out-of-plane vibrational component. This is convenient, for example, in the case of Rayleigh waves. Such measurement abilities are of growing interest, especially for the new challenging configurations of acoustic devices [20,21], including those based on phononic crystals [22–24], nondestructive characterization of surfaces [25,26] or measurements of superficial fields of residual stress [27,26,28].

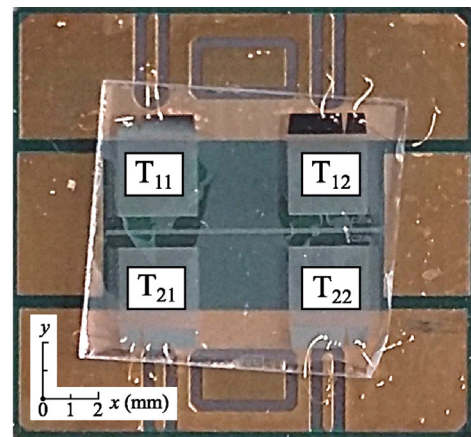
There exist two main types of optical probing devices: scanning and full-field. A full-field laser ultrasonic imaging method measures acoustic motion at a surface without scanning. Images are recorded at normal video frame rates using dynamic holography with photorefractive interferometric detection [29]. In general, the full-field method is significantly faster (even 100×) than scanning approach, but typically the minimum detectable amplitude (from 10s to 100s pm) is not nearly as good as what can be achieved with a scanning probe. The other type of laser Doppler vibrometers is single-point devices which obtain spatial images with mechanical or optical scanning. They are able to provide an extremely high vibration amplitude resolution (up to 0.3 pm [30]). It is worth mentioning that due to their complexity and limited domain of application, laser vibrometers remain mainly “homemade” precision instruments used by a limited number of research groups. We note that there are very few laser Doppler vibrometers capable of operating at ultra-high frequencies available commercially.

This paper focuses on the acquisition and representation of scanning LDV data. Generally the two main approaches of vibrometry data are split into frequency and time domains. On the one hand, Fourier transform methods (viz frequency domain) provide a decomposition of the measurement data into different wave components. This enables easier analysis of complex wave fields, as the constituent waves with different wavelengths and propagation directions can be separated and quantified. This is of special interest for characterization of steady field patterns as for acoustic resonators [31–33]. On the other hand, the devices based on the wave pulse propagation are better analyzed in the time domain, as several transition phenomena are easier to observe and analyse. This specifically involves characterizing phononic crystals [34,35] and anisotropic propagation [22,36]. Within the framework of these directions, we focus on vibrometry data acquisition protocols, imaging of SAW propagation and crosstalk detection on crystals in time domain.

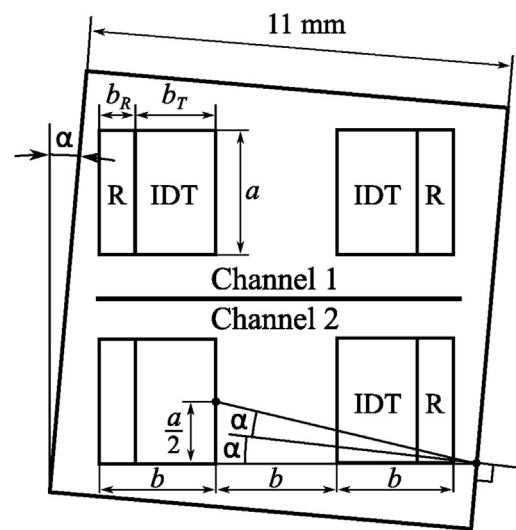
## 2. Design and principle

The device under test represents a gas sensor based on a double-channel electroacoustical delay line [37]. Each delay line consists of identical pair interdigital transducers (IDT). In Fig. 1(a), we label IDTs,  $T_{11}$  and  $T_{12}$  for the 1st channel and  $T_{21}$  and  $T_{22}$  for the 2nd channel. One of the channels is intended to be a reference while the other interacts with a functionalized layer thus providing sensitivity to the presence of targeted gas molecules. The phase difference between two signals corresponds indirectly to a measurement. A double-channel configuration avoids incidental errors due to variations in ambient temperature and humidity.

AT-cut quartz has been selected for the substrate, first because its first order temperature coefficient of frequency (TCF) is close to zero, yielding frequency temperature compensation for standard room conditions [38], and second because the Rayleigh wave propagation mode corresponding to this substrate provides a high sensitivity in gaseous media [5]. Both generation and detection IDTs of the sensor consist of 52 aluminum split finger pairs with a grating period of 10  $\mu\text{m}$ . The wavelength is 40  $\mu\text{m}$ , yielding a frequency



a)



b)

Fig. 1. Illustration of SAW resonator: (a) delay line principle layout; (b) Rayleigh surface acoustic wave.

operation in the vicinity of 78 MHz as the wave velocity approaches 3150 m/s [38].

On the back side of each emitter/receiver IDT, a second short-circuit IDT is placed (20.5 electrode pairs, ‘R’ in Fig. 1), which serves to reflect undesirable waves emitted in the direction opposite to the receiver. Another measure taken to diminish the undesirable reflections is the inclination of the substrate. An inclined substrate edge permits the redirection of reflections from its boundaries in such a way that they do not return to the emitting transducer. The inclination angle  $\alpha$  is chosen to satisfy the condition that the reflected signal returns to the middle of the aperture of the emitting IDT. It can be expressed as:  $\alpha \approx (1/2) \arctan(a/4b) \approx 5^\circ$ , where  $a = 3$  mm is the aperture, and  $b = 3.2$  mm is the length of both the IDT and reflector. In this configuration,  $b$  is also equal to the distance between two IDTs ( $T_{11}$  and  $T_{12}$  or  $T_{21}$  and  $T_{22}$ ), while the IDT length  $b_T$  is equal to 2 mm and the reflector length  $b_R$  is 1.2 mm. The sensor substrate size is 11 mm  $\times$  11 mm. It contained no sensitive layer in order to avoid additional sources of SAW deviations.

## 3. Results and discussion

### 3.1. Simulations result

Heuristic unidimensional models such as (coupling of modes, COM) [39] or mixed matrix [40] are of proven efficiency in terms of predicting device resonance frequency, insertion losses and other

SAW device transfer function characteristics. Parameters for COM computations are often provided by a two-dimensional finite element method (FEM) simulation of a half period of infinite periodic structures (electrode gratings) [41]. Nevertheless, while approaching the real conditions of SAW device realization and operation several additional considerations should be taken into account. For example, introducing of SAW guidance or confinement structures, propagation mode conversions as well as wave reflections which can distort initially calculated device response. In such case, the use of 3D FEM analysis is needed [42]. Additionally, one has to perform a three-dimensional FEM analysis when the device substrate exhibits a two-dimensional asymmetry, which is the case for the sensor shown in Fig. 1.

Although, modern computing power allows the successful modelling of some full-size SAW device configurations in 3D [42], modelling the device under consideration is in not straightforward due to the rather large substrate area and the presence of two channels that can interact. The limiting criterion for the modelling is the fine mesh needed for solving the wave equation (at least 6–10 elements per wavelength [43]). As an example, for a 11 mm × 11 mm × 0.5 mm delay line operating with a 40 μm wavelength, for 4 μm average mesh step we would obtain almost 10<sup>9</sup> elements. Depending on the solver, this can require a few hundred gigabytes (GBs) of memory or even more. Thus a 3D FEM modelling of the full-sized sensor presented in the preceding section would require advanced computing facilities.

To highlight this, we present an example of a simplified 3D FEM simulation with COMSOL Multiphysics of a SAW device with 3 aluminum finger pairs placed on AT-quartz 850 μm × 435 μm × 40 μm substrate (Fig. 2(a)). The IDTs are merely modeled as electrical boundary conditions on the substrate's surface [44]. By means of piezoelectric equations, a sinusoidal tension  $V$  (ac voltage) is imposed as a boundary condition on the electrodes as follows:  $V = V_0 \sin(2\pi f t)$ , where  $V_0$  is the peak voltage,  $f$  is the frequency and  $t$  is the time. Perfectly matched layers (PMLs) [45] are applied along of the SAW device in order to cancel out undesired reflections and to simulate a semi-infinite space. Even this simplified model required more than 45 GB of memory (1.4 × 10<sup>6</sup> degrees of freedom) and took more than 10 h to solve on a 16 core processor.

Fig. 2(b) depicts the electric potential on the surface at  $t = 20.3$  ns, Fig. 2(c) shows the out of plane mechanical displacement on the surface at  $t = 21.1$  ns. For 10 Vpp magnitude applied at the three finger pair input IDT out-of-plane displacements of ~22 pm were observed. This value is compatible with SAW detection by LDV (see LDV sensitivity consideration below) taking into account that it would be greater for 52 electrode pairs of the real sensor [46]. The illustrated limitations of 3D FEM simulation is one of the reasons that SAW device experimental characterization with electrical measurements and optical probing are so important.

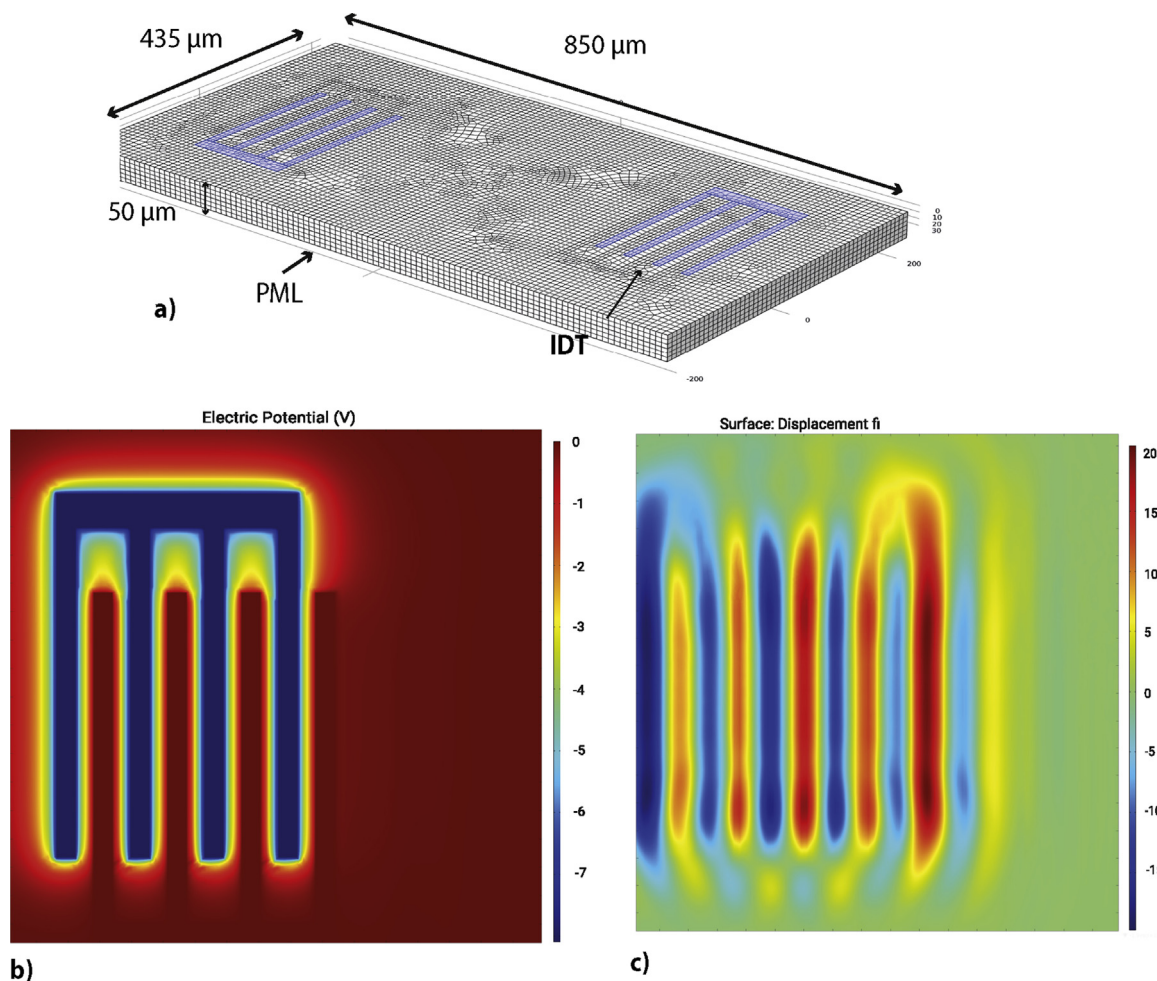


**Fig. 2.** FEM simulation of an electro-acoustic device. (a) Simplified device geometry and simulation mesh; (b) electric potential on the surface at  $t = 20.3$  ns; (c) out of plane mechanical displacement at  $t = 21.1$  ns.

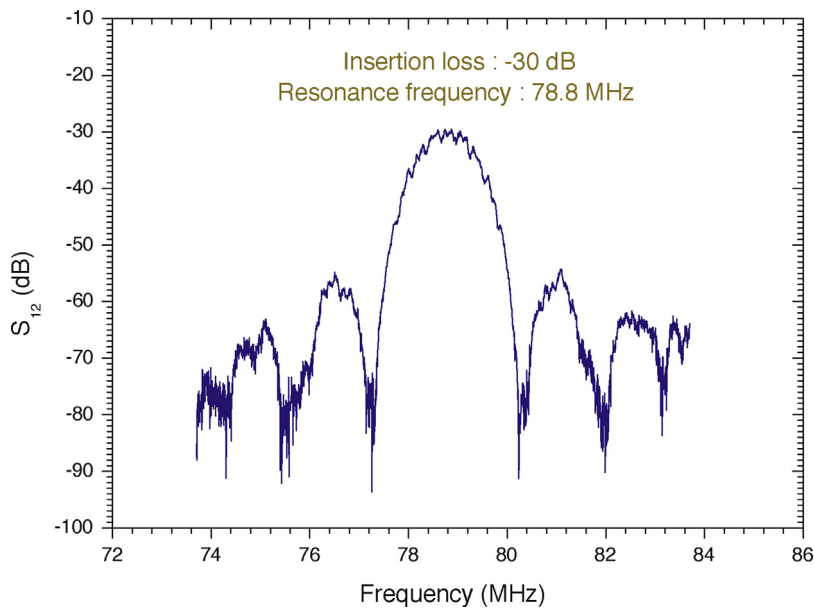


Fig. 3. Frequency response of the SAW device. Synchronous resonance appears at 78.8 MHz.

### 3.2. Radio frequency measurement

Electrical parameters such as insertion losses, operating frequency obtained using network analyzers are typically employed to characterize SAW devices. These measurements were performed in ambient conditions with a vector network analyzer (ZNB 8, Rohde & Schwarz). Fig. 3 shows the frequency response for the 1st mode of the SAW device at 78.8 MHz, with an insertion loss of about  $-30$  dB. Knowing the operating frequency and insertion loss is usually sufficient for a number of applications with conventional well studied IDT configurations. However, these valuable data correspond indirectly to the acoustical field propagating in the device and cannot provide insights into the exact sources of possible problems such as energy escaping from a resonator or unexpected deviations of acoustical pulses. In the next section, we will go into more detail on this subject.

### 3.3. LDV measurement

#### 3.3.1. Measurement setup

The LDV characterization has been performed with a commercial scanning heterodyne Polytec UHF-120 vibrometer. The apparatus allows measurements in the DC to ultra-high frequencies (1.2 GHz) range. The scanning resolution is defined by the motorized stages and is equal to 300 nm. Accordingly to the device datasheet, its SAW amplitude sensitivity threshold which depends on the signal-to-noise ratio (SNR) is defined as  $30 \text{ fm} \cdot \sqrt{\text{Hz}}$ . This gives a low value of 268 pm for a single measurement at 78.8 MHz and dictates the necessity to use averaging. Thus, the sensitivity can be improved proportionally to the square root of the average sweeps number. For the 128 average factor set in all experiments reported below this results in a value of 23 pm. Finally, the bandwidth limit of 200 MHz realized with a zero-phase low-pass digital filter in the Polytec PSV 9.2 software allowed to additionally increase the sensitivity up to  $\sim 10$  pm.

In order to obtain the maximum SAW amplitude and SNR, it is necessary to adapt the sensor excitation signal to the IDTs configuration. An impulse response of a uniform non-apodized IDT represents a sinusoidal burst with the number of cycles equal to the number of constituting electrode pairs [46]. The response to any excitation can be obtained by its convolution with the impulse

response. The maximum corresponds to the autocorrelation function, i.e. to the case when the number of cycles in the sinusoidal burst excitation is equal to the number of cycles in the impulse response. Convolution of these signals will produce a triangular-shaped signal with the duration equal to  $2\Theta$ , where  $\Theta$  is the duration of the excitation burst. A further increase of the excitation time by multiplying the number of cycles is not reasonable as it will produce a trapezoidal-shaped response with no gain in amplitude.

All of the experimental results reported below were obtained with 52 cycles of 78.8 MHz sinusoidal burst excitation. This allowed to achieve a rather high SAW amplitude (approximately of 0.5 nm) and a satisfactory signal-to-noise ratio (34 dB). In all cases, the IDT  $T_{21}$  was set to be an emitter.

#### 3.3.2. LDV data presentation methods

Initially, an LDV unit provides measurement data on out-of-plane surface motion at a single point (Fig. 4(a-c)). Each point measurements corresponds to an A-scan [47]. Elementary A-Scan waveforms allow the estimation of several important characteristics of a test sample, but generally are of low value as a comprehensive analysis and the presentation of signal evolution is not available. By adding a scanning feature to the LDV setup one obtains a way to extend the A-scan presentation to B- or C-scans, and obtain much more information.

For 1D line scanning, one changes the graphical presentation of the waveform type presentation on an A-scan (Fig. 4(a-c)) to color-scaled lines referenced at each scanning point. Measurement data are presented as a 2D colormap image relating signal evaluation in time and spatial domains (Fig. 4(e)). This presentation method is known as the B-Scan. It is convenient for characterizing linear objects, e.g. for rails in the case of macroscopic nondestructive testing [47] or for visualizing body cross-sections in medical applications [48].

AC-scan representation is used while performing a 2D scan over an object area. Measured signal values corresponding to a specified time instant are represented in a 2D format in reference to the object's geometrical coordinates. For numerous engineering and medical applications A-Scan time instants are recalculated in terms of the probing wave penetration distance. Thus, C-scans are represented as a series of slices referenced to the probing depth [48]. In

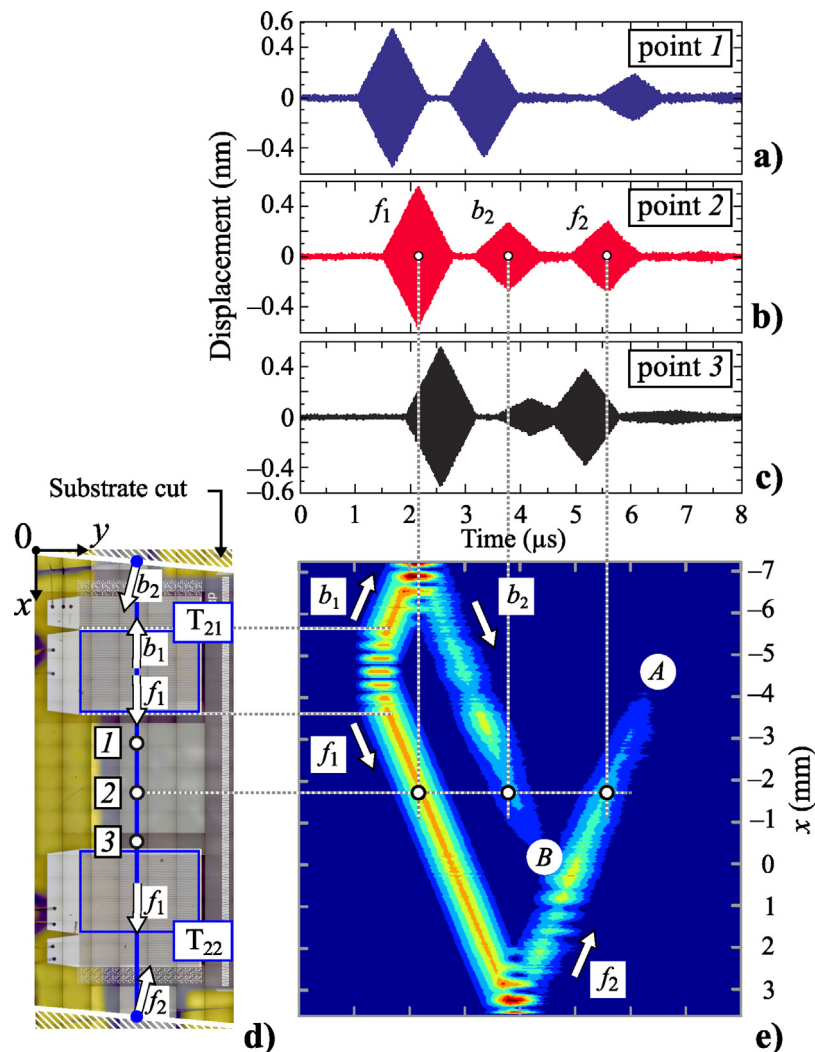


**Fig. 4.** A-Scan data and its interpretation: (a), (b), (c) three A-Scan waveforms corresponding to different points on the axis between  $T_{21}$  and  $T_{22}$ ; (d) microscopic image of the SAW sensor measurement channel 2; (e) B-Scan image taken along the same axis as the A-Scans.

the study described below, C-scans correspond directly to different time shots revealing wave propagation on the sensor's substrate and forming a sort of video frames sequence.

### 3.3.3. A-Scan

LDV data in a form of A-Scan waveforms for three measurement points situated between emitter and receiver of the sensor are presented in Fig. 4(a-c). The corresponding points '1', '2', and '3', are shown on the microscopic image of sensor in Fig. 4(d). A first analysis reveals a high level of boundary echoes, but a consistent interpretation of all the measured pulses is possible only with the additional calculations of the arrival delays, which take into account the device geometry.

In order to provide an explanation of this behavior, we include in Fig. 4(e) a B-scan image relating time domain measurements to the object's geometry. The scanned region is depicted by a blue straight line in Fig. 4(d), and each line of the B-Scan contour plot represents a time domain measurement and is tied to a geometrical point where it was taken. To improve the visualization, the waveform envelopes are displayed instead of the raw waveform points.

An example of an echoes interpretation is given for the point 2 situated in the middle between the emitting and receiving transducers  $T_{21}$  and  $T_{22}$  respectively. In Fig. 4(d), the forward-emitted (in the direction of the  $T_{22}$  transducer) pulse is referred to as ' $f_n$ '

and the backward-emitted pulse is depicted as ' $b_n$ '. The indexes  $n$ , such as  $f_1$  or  $b_2$ , correspond to the number of reflection from the substrate boundary (highlighted by the hatching areas). If we take a line corresponding to the point '2' coordinate in Fig. 4(d), it becomes evident that the A-scan waveform in Fig. 4(b) represents a sequence of  $f_1$ ,  $b_2$  and  $f_2$  pulses. The remaining figures represent different sequences of these pulses as well. The regions depicted as 'A' and 'B' in Fig. 4(e) do not correspond to the attenuation of the signal but to the outing of the pulses from the scan line due to the substrate inclination. This particularity of the sensor functioning will be studied further.

### 3.3.4. C-Scan

Considerably more insight on the wave propagation can be achieved in a 2D C-Scan mode. The main issue when performing a C-Scan mapping consists in scan mesh definition. In the studied case, obtaining spatially resolved signal waveforms is not practical as it demands the acquisition of several points per period, which can be achieved only with very dense scan meshes. In order to diminish the number of scan points, the C-Scan is constructed basing on the signal envelope values. For this reason, we define the scan mesh geometrical resolution based on the target parameter which is the "number of scan points per signal envelope". This parameter was set to the value of 20 points per envelope as such a

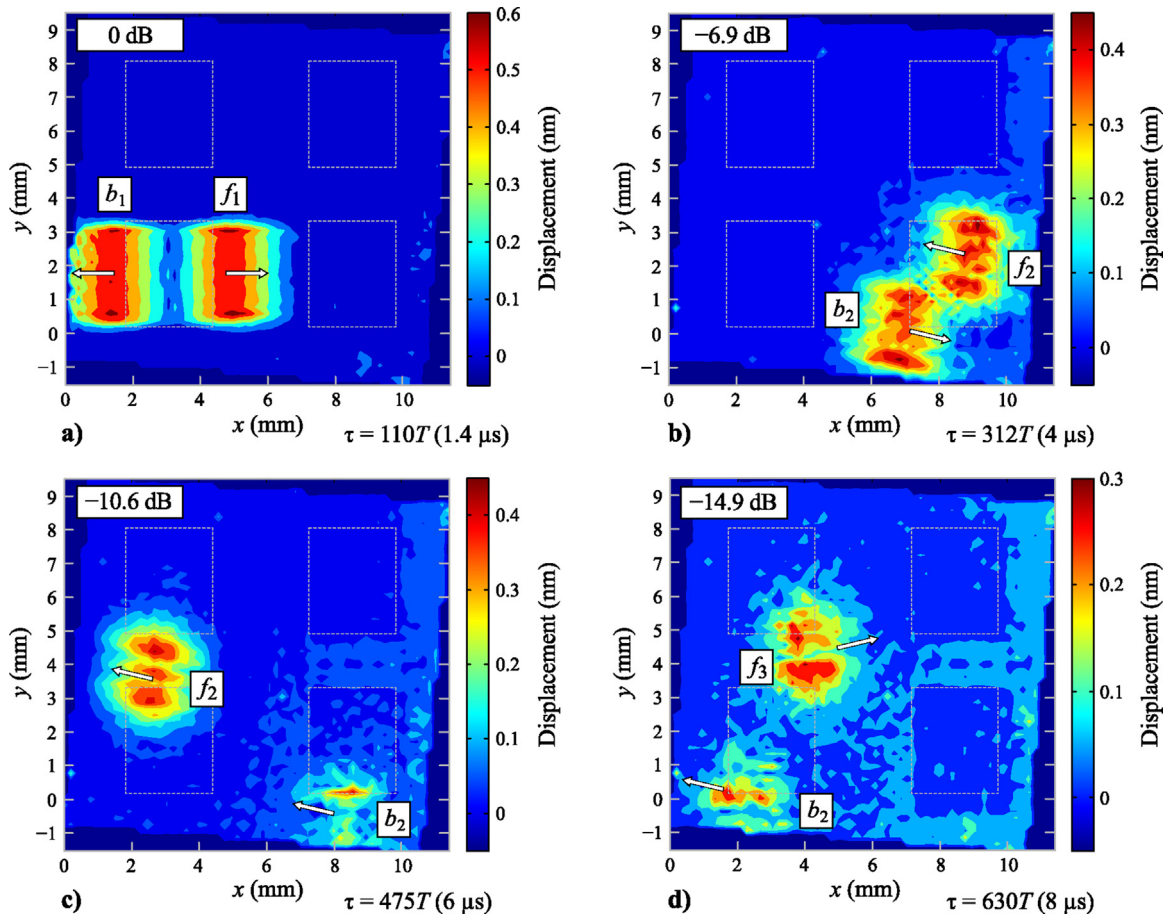


Fig. 5. C-Scan data at different time instants.

value permits the restoration of the signal shape with good quality [43]. Based on this target parameter the definition of scan resolution is straightforward. The duration of the triangle-shaped pulse emitted by  $T_{21}$  is equal to  $1.32 \mu\text{s}$  (double duration of the excitation signal, Fig. 4(a-c)). A sound velocity value of  $3159 \text{ m/s}$  at AT-cut quartz [48], corresponds in the spatial domain to the signal's envelope length of  $4 \text{ mm}$ . Imposing the target parameter to 20 points per envelope, we obtain spatial scan step value of  $200 \mu\text{m}$ . Dividing the substrate area  $11 \text{ mm} \times 11 \text{ mm}$  by the scan cell area  $0.2 \text{ mm} \times 0.2 \text{ mm}$  we obtain a scan mesh consisting of 3025 points. In experimental conditions the mesh resolution was decreased to  $190 \mu\text{m} \times 190 \mu\text{m}$  as some margin from substrate border had to be introduced. The same number of 3025 scan points was maintained. We chose to average 128 sweeps, one acquisition took about 12 s, which results in a duration of 10.2 h for the complete C-Scan.

C-Scan data corresponding to different time instances are shown in Fig. 5. As already mentioned above, in all experiments the SAWs are emitted by the  $T_{21}$  transducer (Fig. 1). The images here are presented in a relative colormap scale (individual colormap for each image), because with an absolute colormap the weak signals would become indistinguishable. The meaning of the pulse tags ' $f_n$ ' or ' $b_n$ ' is the same as for the B-Scan image in Fig. 4(e). For each time shot the attenuation value of total signal energy relative to the emission instant (Fig. 5(a),  $\tau_0 = 1.4 \mu\text{s}$ ) is shown.

At the first instant (Fig. 5(a))  $\tau_1 = 1.4 \mu\text{s}$  corresponding to 110 cycles of excitation, the typical IDT bidirectional emission is visible. After, we observe the full reflection of the both SAW pulses from the inclined substrate boundaries (Fig. 5(b),  $\tau_2 = 4 \mu\text{s}$  corresponding to 312 cycles of excitation). The consequent moments  $\tau_3 = 6 \mu\text{s}$  and  $\tau_4 = 8 \mu\text{s}$  show additional reflections of the pulses at the sub-

strate boundaries leading to change of direction of the two initially parallel beams (Fig. 4(c, d)). No signals reflected from the backside of the IDT electrodes (depicted in Fig. 1(b) as 'R') are detected on these images.

One can notice from Fig. 5 that the directly emitted pulse  $f_3$  penetrates in the zone of the second measurement channel leading to a crosstalk issue. We see the confirmation of reciprocal channel coupling by the acoustical test (Fig. 6) which consists in measuring the voltage in receiving IDTs with an oscilloscope. The crosstalk value from the acoustical measurement corresponds well with the attenuation measured with the C-Scan. The  $\tau_4 = 8 \mu\text{s}$  time instant shown in Fig. 5(d) corresponds to the beginning of the arrival of  $f_3$  pulse at  $T_{12}$  transducer and its energy attenuation is  $-14.9 \text{ dB}$ . The acoustical signal for the same transducer is attenuated by  $-15.2 \text{ dB}$  in reference to signal at  $T_{22}$ .

With the evident advantage of the C-Scan technique such as the complete insight into the device behavior, we note also certain disadvantages. First, the 2D surface scanning is time-consuming. For example, even with the rather moderate spatial resolution reported above, the C-Scan takes about 10.2 h. Second, when a relative colormap scale is used, the representation of the signal attenuation between different time instants is graphically complicated. Finally, it can be hard to present the dynamics of the process in static images on paper as we are limited at series of instantaneous shots.

### 3.3.5. B-Scan

3.3.5.1. IDT directivity measurement. Initially intended for linear objects, the B-Scan in its multi-line implementation can also be used to visualize wave propagation on a surface. First of all, a series of B-Scans permits to quantify the directivity of IDT emission. The

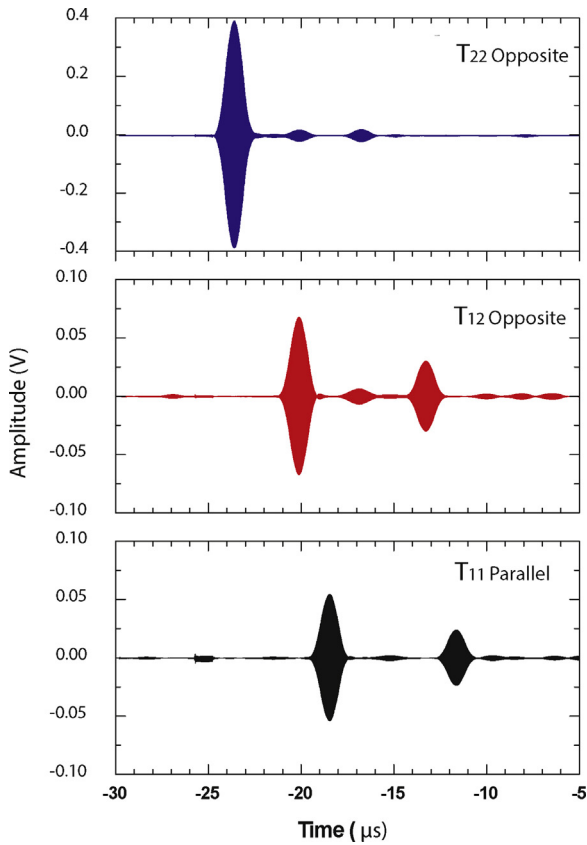


**Fig. 6.** Acoustically detected crosstalk of the SAW sensor. The  $T_{21}$  transducer is the emitter and the response of three other available transducers is presented (the opposite transducer  $T_{22}$  in the 2nd channel, and the transducers from the 1st channel:  $T_{12}$  and  $T_{11}$ ).

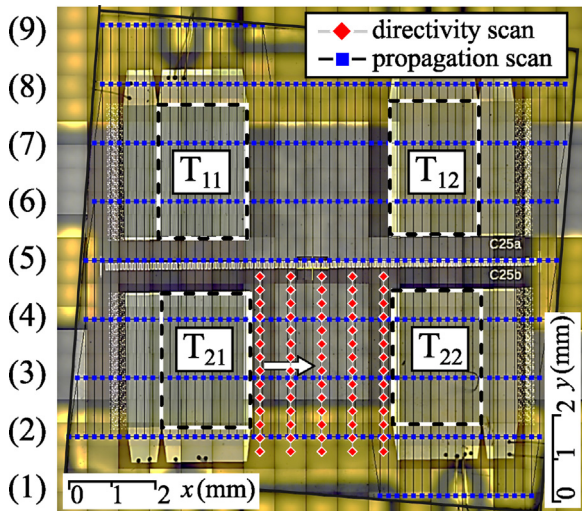


**Fig. 7.** Scanning grid for multi-line B-scans. Red diamonds correspond to the directivity characterization and blue squares correspond to propagation mapping mesh. Scan line numbers for the latter measurements are displayed on the left of the figure. (For interpretation of the references to color in this legend, the reader is referred to the web version of the article.)

C-Scan in Fig. 5 indicates already that divergence is not significant, but a B-Scan measurement allows its quantification.

The directivity patterns have been measured on 5 parallel scan lines separated by  $765 \mu\text{m}$  step (Fig. 7, scan points are displayed by red diamonds). The lines are oriented normally to the direction of wave propagation between the emitting transducer  $T_{21}$  and the

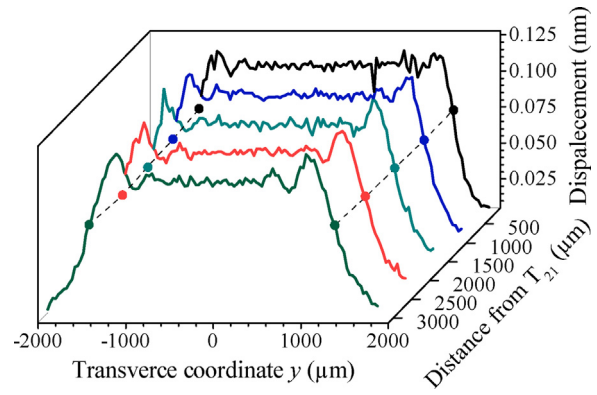


**Fig. 8.** Directivity pattern of the emitting transducer  $T_{21}$ . Circles connected by dashed lines correspond to intersections with the  $-3 \text{ dB}$  level for each profile.

receiver  $T_{22}$ . The first line is situated near the emitter  $T_{21}$  within  $70 \mu\text{m}$ , and the last one is close to the receiver  $T_{22}$ .

The measurement results reported in Fig. 8 reveal that for  $T_{21}$  there is neither emission divergence nor beam steering [49]. Both of these phenomena are considered as undesired as they lead to signal power loss at receiving IDT. The absence of divergence is explained by the operation in near field, in other words in the range of the Fresnel distance  $x_f$ . The Fresnel distance can be found from the equation [49]:

$$x_f \approx \frac{a^2 k_0}{10\pi} \left| 1 + \frac{\delta y}{\delta \Psi} \right| \quad (1)$$

where  $a$  is the transducer aperture,  $k_0$  is the wave vector equal to  $\omega/c$ , and  $\delta y/\delta \Psi = 0.653$  is the diffraction coefficient whose value can be found in [38]. For the current aperture  $a = 75$  wavelengths, we obtain a Fresnel distance of  $27 \text{ mm}$ .

The beam steering phenomenon can occur in anisotropic materials. It represents the case of wave propagation in a direction that is not normal to the wavefronts [49]. It was avoided by the exact alignment of SAW propagation direction with the crystalline axis of the AT quartz substrate [50].

**3.3.5.2. SAW propagation visualization.** At the second step of the B-Scan characterization, an attempt to obtain the insight about the SAW propagation at the whole substrate area has been done. The goal was achieved by a series of B-Scans along distant lines covering all region of interest. The mesh grid chosen for the series of B-Scans is presented as blue squares in Fig. 7. The  $x$ -resolution rested unchanged comparing to the C-Scan and equal to  $\delta x = 190 \mu\text{m}$ , while the  $y$ -resolution has been set in order to achieve the condition  $\delta y \approx a/2 = 1.3 \text{ mm}$  (equal to half of the aperture, see Fig 1 (b)). Such a value for the  $y$ -resolution was chosen arbitrarily in order to obtain three values of beam attenuation per aperture and to find an averaged value. Further consideration will show that such an approach allowed an accurate estimation of the crosstalk value. In all, the scan mesh consisted of 9 scan lines containing 434 points. With the same signal acquisition settings as for the C-Scan, the multi-line B-Scan was accomplished in 90 min.

The data obtained for this series of B-Scans are presented in Fig. 9. The meaning of the indexes ' $f_n$ ' and ' $b_n$ ', is the same as for the case of the B-Scan in Fig. 4(e). As in the case of the C-Scan, the multi-line B-Scan provides evidence of the reflections from substrate boundaries. The signal level evaluation during the propagation on a scan line is easier to represent, however graphical data becomes detached from the geometry of the device, i.e. it becomes less intuitive.

In order to improve the data perception, the reflection pattern could be presented as a series of B-Scans tied to the sensor geome-



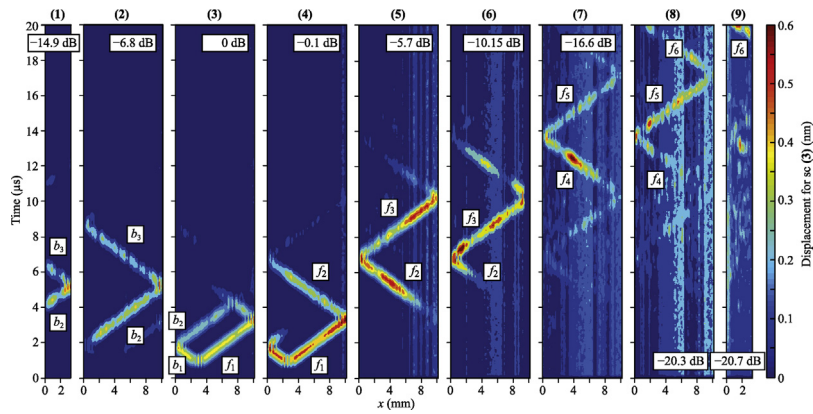


Fig. 9. Multiline B-Scan (numbers on the top correspond to the scan lines shown in Fig. 8).

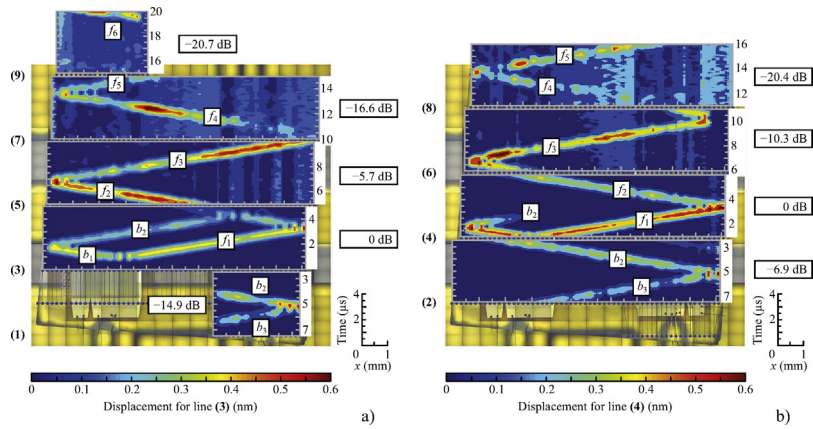


Fig. 10. Two series of geometrically tied B-scans for interleaving scan lines.

try. Taking into account the absence of divergence (Fig. 8) in emitted pulses, for representation it is better to choose the scan lines that are more distant than the IDT aperture ( $a$  in Fig. 1). In this case, the signal leaves one scan line and immediately enters into another. Thus, the signals do not overlap and the graphical interpretation of the information becomes easier. As a result, the scanning mesh in Fig. 8 contains 2 times more scan lines than necessary and this reduced scan could be accomplished in 45 min. Fig. 10 shows that this gives the same insight into the SAW propagation on the device substrate as in Fig. 9, while making the visual information easier to interpret. We can estimate the crosstalk by analyzing scan lines that cover the second measurement channel. These are lines '6', '7' and '8' in Fig. 7. The mean value of attenuation for these lines is  $-15.7$  dB which corresponds well to the acoustical and C-Scan measurements.

#### 4. Discussion

The optical probing reveals two issues of the current sensor design. First, we observe undesired reflections from the borders of the substrate. The inclined edge of the substrate efficiently evacuates the reflected signal from the measurement channel but it leads to the crosstalk issue. The second revealed issue is the inefficiency of the backside IDT reflectors. This may be caused by the split electrode geometry which are the same as for the emitters. Also, we observe that acoustical measurements, C-Scan and multiline B-Scan provide similar crosstalk value estimations. These observations give an exact indication of the ways that the performance of the sensor can be improved. We have provided a demonstration of the main modes of scanning LDV data acquisition and presentation:

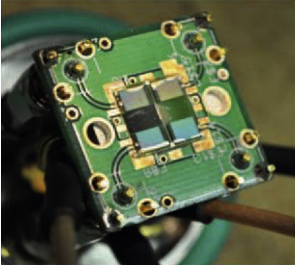
- A-Scan is a rapid technique permitting the detection of the possible unwanted reflections or other abnormalities while the exact reasons of device dysfunction remain difficult to ascertain.
- C-Scan provides a complete insight into the acoustic field evolution on the device surface, but acquisition is time-consuming (10.2 h) and dynamic data representation is not straightforward, especially on static supports.
- B-Scan is a convenient mode for the representation of SAW evolution, however, when acquired along a single line, it cannot provide an entire signal propagation history (outing points 'A' and 'B' in Fig. 4). A multi-line B-Scan gives the same amount of information as a C-Scan (beam propagation, directivity and estimation of the crosstalk value) with more versatility for data representation and it requires significantly shorter scanning times (45 min for geometrically tied B-Scan).

The reduction of scanning time can be also profitable for the detection of weak signals since it gives an opportunity to increase the data acquisition averaging rate. So, the multiline B-Scan should be considered as the optimized protocol for fast SAW device characterization in the time domain. Table 1 summarizes the results of this analysis.

#### 5. Conclusion

This paper provides the basis to predict the behavior of high-frequency SAW devices, which should facilitate the design and optimization of technologically useful piezoelectric structures and improve the understanding of high-frequency surface acoustic waves in general. These time-domain measurements allow visu-

**Table 1**  
Summary of the measured value of the SAW.

Parameters	SAW	Advantages/drawbacks
<i>Geometry</i>		<i>Photography</i>
Dimensions (mm)	11 × 11 × 0.5	
Finger width (μm)	10	
Finger space (μm)	10	
Wavelength (μm)	40	
Aperture (μm)	3000	
Number of fingers (pairs)	52.5	
Propagation length (mm)	3.2	
<i>Simulation</i>		
Dimensions (μm)	850 × 435 × 40	
Number of fingers (pairs)	3	++ Magnitude displacement
Duration	10 h	– Not complete insight
<i>Electrical</i>		
Resonance frequency $f_0$	78.8 MHz	++ Loss measurement
Duration	15 min	– Not complete insight
		++ Fast
<i>LDV measurement</i>		
Excitation	52 cycles	++ Complete insight
		++ Non-contact
<i>A-Scan</i>		
Duration	30 s	++ Magnitude displacement
		– Presence of echoes
<i>C-Scan</i>		
Total scan points	3025	
Resolutions	190 × 190 μm	++ Dynamic information
Duration	10.2 h	– Time costly
<i>B-Scan</i>		
Number of scan lines	9	
Total scan points	434	
Resolutions	190 μm × 1.3 mm	++ Static information
Duration	45–90 min	++ Fast

alization of the wave propagations in SAW devices, detection of loss sources, unwanted responses or acoustic crosstalk. Multiline B-Scan allows detection of the same amount of information as compared to the C-Scan: visualization of beam propagation, directivity and estimation of the crosstalk value. The testing time, however, can be considerably reduced from 10 h for the C-Scan to 45 min for the geometrically referenced multi-line B-Scan. In addition, the B-scan series permit to better represent the progression of the signal during the entire time of the analysis. When presented on paper, static information from B-Scans could be advantageous compared to a dynamic video frame sequence obtained with a C-Scan. We conclude that simulations and radiofrequency measurements combined with detailed laser interferometric measurements provide a wealth of information for industrial SAW device R&D purposes in such fields as microelectronic, phononic and acoustic trapped energy resonators. In the future, it should also be possible to extend these experimental protocols and numerical methods to the analysis of SAW devices based on different piezoelectric substrates exhibiting more complicated acoustic field behavior and operating at different frequency ranges.

## Acknowledgements

The authors acknowledge the clean room and characterization laboratories staff at FEMTO-ST, IEMN and C2N. This work was partly supported by the French RENATECH network and its technological facilities. The work has been accomplished with the support of the ELSAT2020 project co-financed by the European Union with the

European Regional Development Fund, the French state and the Hauts de France Region Council.

## References

- [1] D.R. Morgan, Surface acoustic wave devices and applications, *Ultrasonics* 11 (3) (1973) 121–131, [http://dx.doi.org/10.1016/0041-624X\(73\)90608-2](http://dx.doi.org/10.1016/0041-624X(73)90608-2).
- [2] F. Ananasso, Review of saw devices and their signal processing applications in space communications, *Int. J. Satell. Commun.* 7 (4) (1989) 235–261, <http://dx.doi.org/10.1002/sat.4600070404>.
- [3] D.P. Morgan, History of SAW devices, *Proceedings of the 1998 IEEE International Frequency Control Symposium (Cat. No. 98CH36165)* (1998) 439–460.
- [4] H. Wohltjen, R. Dessy, Surface acoustic wave probes for chemical analysis. II. Gas chromatography detector, *Anal. Chem.* 51 (9) (1979) 1465–1470, <http://dx.doi.org/10.1021/ac50045a025>.
- [5] H. Wohltjen, R. Dessy, Surface acoustic wave probe for chemical analysis. I. Introduction and instrument description, *Anal. Chem.* 51 (9) (1979) 1458–1464, <http://dx.doi.org/10.1021/ac50045a024>.
- [6] Z.P. Khlebarov, A.I. Stoyanova, D.I. Topalova, Surface acoustic wave gas sensors, *Sens. Actuators B: Chem.* 8 (1) (1992) 33–40, [http://dx.doi.org/10.1016/0925-4005\(92\)85005-H](http://dx.doi.org/10.1016/0925-4005(92)85005-H).
- [7] W.E. Bulst, G. Fischerauer, L. Reindl, State of the art in wireless sensing with surface acoustic waves, *IEEE Trans. Ind. Electron.* 48 (2) (2001) 265–271, <http://dx.doi.org/10.1109/41.915404>.
- [8] M. Brandl, T. Posniecek, K. Kellner, Position estimation of RFID-based sensors using SAW compressive receivers, *Sens. Actuators A: Phys.* 244 (2016) 277–284, <http://dx.doi.org/10.1016/j.sna.2016.04.032>.
- [9] W. Wang, K. Lee, I. Woo, I. Park, S. Yang, Optimal design on SAW sensor for wireless pressure measurement based on reflective delay line, *Sens. Actuators A: Phys.* 139 (12) (2007) 2–6.
- [10] Y. Zhu, Y. Zheng, C. Sun, Y. Gao, A.Y. Gu, H. Campanella, A high-impedance dual-mode SAW resonator for ultra low power and high data rate FSK modulator, *Sens. Actuators A: Phys.* 220 (2014) 188–193, <http://dx.doi.org/10.1016/j.sna.2014.10.001>.

- [11] V. Plessky, J. Koskela, Coupling-of-modes analysis of SAW devices, *Int. J. High Speed Electron. Syst.* 10 (4) (2000) 867–947, <http://dx.doi.org/10.1142/S0129156400000684>.
- [12] W. Soluch, Design of SAW delay lines for sensors, *Sens. Actuators A: Phys.* 67 (1) (1998) 60–64.
- [13] C. Fu, O. Elmazria, F. Sarry, T. Mahalingam, S.S. Yang, K. Lee, Development of wireless, battery-free gyroscope based on one-port SAW delay line and double resonant antenna, *Sens. Actuators A: Phys.* 220 (2014) 270–280, <http://dx.doi.org/10.1016/j.sna.2014.10.006>.
- [14] K. Kokkonen, Laser interferometers in physical acoustics, in: 2009 IEEE International Ultrasonics Symposium, 2009, pp. 1036–1043, <http://dx.doi.org/10.1109/ULTSYM.2009.5441587>.
- [15] R. Whitman, A. Koppel, Probing of acoustic surface perturbations by coherent light, *Appl. Opt.* 8 (8) (1969) 1567–1576.
- [16] E. Herth, F. Lardet-Vieudrin, L. Valbin, E. Algr, Detecting response of square and circular Si/AlN/Al membranes transducers by laser vibrometry Doppler and impedance meter, 2015 Symposium on Design, Test, Integration and Packaging of MEMS/MOEMS (DTIP) (2015) 1–5, <http://dx.doi.org/10.1109/DTIP.2015.7160996>.
- [17] E. Herth, F. Lardet-Vieudrin, F. Deux, L. Valbin, E. Algr, J. Schell, H. Steger, Detection of out-of-plane and in-plane (XYZ) motions of piezoelectric microcantilever by 3D-laser Doppler vibrometry, 2016 Symposium on Design, Test, Integration and Packaging of MEMS/MOEMS (DTIP) (2016) 1–4, <http://dx.doi.org/10.1109/DTIP.2016.7514876>.
- [18] E. Herth, F. Lardet-Vieudrin, L. Valbin, G. Lissorgues, Mechanical behavior of T-shaped AlN membrane based on thin film elongation acoustic resonator, 2016 Symposium on Design, Test, Integration and Packaging of MEMS/MOEMS (DTIP) (2016) 1–4, <http://dx.doi.org/10.1109/DTIP.2016.7514867>.
- [19] P. Castellini, G. Revel, E. Tomasini, Laser Doppler vibrometry: a review of advances and applications, *Shock Vib. Digest* 30 (6) (1998) 443–456.
- [20] E. Herth, L. Valbin, F. Lardet-Vieudrin, E. Algr, Modeling and detecting response of micromachining square and circular membranes transducers based on AlN thin film piezoelectric layer, *Microsyst. Technol.* (2015) 1–8, <http://dx.doi.org/10.1007/s00542-015-2727-9>.
- [21] E. Herth, E. Algr, J.-Y. Rauch, J.-C. Gerbedoen, N. Defrance, P. Delobelle, Modeling and characterization of piezoelectric beams based on an aluminum nitride thin-film layer, *Phys. Status Solidi A* 213 (1) (2016) 114–121.
- [22] Y. Sugawara, O.B. Wright, O. Matsuda, M. Takigahira, Y. Tanaka, S. Tamura, V.E. Gusev, Watching ripples on crystals, *Phys. Rev. Lett.* 88 (18) (2002) 185504, <http://dx.doi.org/10.1103/PhysRevLett.88.185504>.
- [23] J. Meltaus, S.S. Hong, O. Holmgren, K. Kokkonen, V.P. Plessky, Double-resonance SAW filters, *IEEE Trans. Ultrason. Ferroelectr. Freq. Control* 54 (3) (2007) 659–667, <http://dx.doi.org/10.1109/TUFFC.2007.289>.
- [24] S. Benchabane, O. Gaiffe, R. Salut, G. Ulliac, V. Laude, K. Kokkonen, Guidance of surface waves in a micron-scale phononic crystal line-defect waveguide, *Appl. Phys. Lett.* 106 (8) (2015) 081903, <http://dx.doi.org/10.1063/1.4913532>.
- [25] J. Deboucq, M. Duquennoy, M. Ouaftouh, F. Jenot, J. Carlier, M. Ourak, Development of interdigital transducer sensors for nondestructive characterization of thin films using high frequency Rayleigh waves, *Rev. Sci. Instrum.* 82 (6) (2011) 064905, <http://dx.doi.org/10.1063/1.3600797>.
- [26] D. Fall, F. Compoint, M. Duquennoy, H. Piombini, M. Ouaftouh, F. Jenot, B. Piwakowski, P. Belleville, C. Ambar, Surface acoustic wave characterization of optical sol-gel thin layers, *Ultrasonics* 68 (2016) 102–107, <http://dx.doi.org/10.1016/j.ultras.2016.02.006>.
- [27] M. Duquennoy, M. Ouaftouh, J. Deboucq, J.-E. Lefebvre, F. Jenot, M. Ourak, Influence of a superficial field of residual stress on the propagation of surface waves applied to the estimation of the depth of the superficial stressed zone, *Appl. Phys. Lett.* 101 (2012) 234104, <http://dx.doi.org/10.1063/1.4768434>.
- [28] M. Duquennoy, M. Ouaftouh, J. Deboucq, J.-E. Lefebvre, F. Jenot, M. Ourak, Characterization of micrometric and superficial residual stresses using high frequency surface acoustic waves generated by interdigital transducers, *J. Acoust. Soc. Am.* 134 (2013) 4360, <http://dx.doi.org/10.1121/1.4826176>.
- [29] K.L. Telschow, V.A. Deason, D.L. Cottle, J.D. Larson, Full-field imaging of gigahertz film bulk acoustic resonator motion, *IEEE Trans. Ultrason. Ferroelectr. Freq. Control* 50 (10) (2003) 1279–1285, <http://dx.doi.org/10.1109/TUFFC.2003.1244744>.
- [30] J.E. Graebner, Optical scanning interferometer for dynamic imaging of high-frequency surface motion, 2000 IEEE Ultrasonics Symposium, vol. 1 (2000) 733–736, <http://dx.doi.org/10.1109/ULTSYM.2000.922651>.
- [31] N. Wu, K.-Y. Hashimoto, K. Kashiwa, T. Omori, M. Yamaguchi, Study on the frequency dependence of lateral energy leakage in RF bulk acoustic wave device by fast-scanning laser probe system, *Jpn. J. Appl. Phys.* 48 (7) (2009) 07GG01, <http://dx.doi.org/10.1143/JJAP.48.07GG01>.
- [32] H.E. Engan, A. Ronnekleiv, Enhancement of SAW laser probe measurements by signal processing, 1999 IEEE Ultrasonics Symposium, Proceedings, International Symposium (Cat. No. 99CH37027), vol. 1 (1999) 217–220, <http://dx.doi.org/10.1109/ULTSYM.1999.849389>.
- [33] H. Kamizuma, T. Omori, K. Hamishoto, M. Yamaguchi, Development of fast-scanning laser probe system based on knife-edge method for diagnosis of RF surface acoustic wave devices, *IEEE Trans. Ultrason. Ferroelectr. Freq. Control* 53 (6) (2006) 1186–1191, <http://dx.doi.org/10.1109/TUFFC.2006.1642517>.
- [34] D.M. Profunser, O.B. Wright, O. Matsuda, Imaging ripples on phononic crystals reveals acoustic band structure and bloch harmonics, *Phys. Rev. Lett.* 97 (5) (2006) 055502, <http://dx.doi.org/10.1103/PhysRevLett.97.055502>.
- [35] V. Laude, K. Kokkonen, S. Benchabane, Characterization of surface acoustic wave focusing by an annular interdigital transducer, 2009 IEEE International Ultrasonics Symposium (2009) 919–922, <http://dx.doi.org/10.1109/ULTSYM.2009.5441703>.
- [36] V. Laude, K. Kokkonen, S. Benchabane, M. Kaivola, Material anisotropy unveiled by random scattering of surface acoustic waves, *Appl. Phys. Lett.* 98 (6) (2011), 063506-063506-3.
- [37] M. Vanotti, V. Blondeau-Patissier, V. Moutarlier, S. Ballandras, Analysis of palladium and yttrium-palladium alloy layers used for hydrogen detection with SAW device, *Sens. Actuators B: Chem.* 217 (2015) 30–35, <http://dx.doi.org/10.1016/j.snb.2015.02.049>.
- [38] A.J. Slobodnik, Surface acoustic waves and SAW materials, *Proc. IEEE* 64 (5) (1976) 581–595.
- [39] P.V. Wright, Analysis and design of low-loss SAW devices with internal reflections using coupling-of-modes theory, *Proceedings, IEEE Ultrasonics Symposium*, vol. 1 (1989) 141–152, <http://dx.doi.org/10.1109/ULTSYM.1989.66974>.
- [40] G. Tobolka, Mixed matrix representation of SAW transducers, *IEEE Trans. Sonics Ultrason.* 26 (6) (1979) 426–427, <http://dx.doi.org/10.1109/T-SU.1979.31128>.
- [41] M. Buchner, W. Ruile, A. Dietz, R. Dill, FEM analysis of the reflection coefficient of SAWs in an infinite periodic array, *IEEE 1991 Ultrasonics Symposium*, vol. 1 (1991) 371–375, <http://dx.doi.org/10.1109/ULTSYM.1991.234189>.
- [42] S. Zhgoune, D. Tsimbal, A. Shvetsov, K. Bhattacharjee, 3D finite element modeling of real size SAW devices and experimental validation, 2008 IEEE Ultrasonics Symposium (2008) 1932–1935, <http://dx.doi.org/10.1109/ULTSYM.2008.0476>.
- [43] S. Marburg, Discretization requirements: how many elements per wavelength are necessary? in: *Computational Acoustics of Noise Propagation in Fluids*, Springer Edition, Finite and Boundary Element Methods, B. Nolte, Berlin, 2008, pp. 309–332.
- [44] R. Takpara, M. Duquennoy, M. Ouaftouh, C. Courtois, F. Jenot, M. Rguiti, Optimization of SAW-type surface wave ultrasonic sensors for ultrasonic SHM Res. *Nondestructive Eval.* 27 (2016) 1–17.
- [45] J.-P. Berenger, A perfectly matched layer for the absorption of electromagnetic waves, *J. Comput. Phys.* 114 (2) (1994) 185–200, <http://dx.doi.org/10.1006/jcph.1994.1159>.
- [46] D. Royer, E. Dieulesaint, Interdigital-electrode transducers for surface waves *Elastic Waves in Solids: Generation, Acousto-Optic Interaction, Applications*, vol. 2, Springer, Berlin, 2000, pp. 47–135.
- [47] J. Krautkrmer, H. Krautkrmer, Pulse-echo method, in: *Ultrasonic Testing of Materials*, Springer, Berlin Heidelberg, 1983, pp. 193–264.
- [48] J.F. Havlice, J.C. Taenzer, Medical ultrasonic imaging: an overview of principles and instrumentation, *Proc. IEEE* 67 (4) (1979) 620–641, <http://dx.doi.org/10.1109/PROC.1979.11287>.
- [49] D.P. Morgan, Propagation effects and materials, in: *Surface-Wave Devices for signal Processing*, vol. 19 of *Studies in Electrical and Electronic Engineering*, Elsevier, Amsterdam, The Netherlands, 1991, pp. 129–151.
- [50] B.P. Abbott, L. Solie, A minimal diffraction cut of quartz for high performance SAW filters, 2000 IEEE Ultrasonics Symposium. Proceeding of the International Symposium (Cat. No. 00CH37121), vol. 1 (2000) 235–240, <http://dx.doi.org/10.1109/ULTSYM.2000.922547>.